Journal of Materials Chemistry B

ROYAL SOCIETY OF CHEMISTRY

PAPER

View Article Online
View Journal | View Issue

Cite this: J. Mater. Chem. B, 2025, 13, 15309

A multifunctional IL@MOF composite-based hydrogel for enhanced transdermal drug delivery of 5-fluorouracil

Ishani Pandya,[a] Vidhi Joshi,[a] Raviraj Pansuriya,[a] Naina Raje,[b] Mohammed A. Assiri[c] and Naved Malek *[a]

Advances in biomaterial-based transdermal drug delivery systems (TDDSs) are unlocking new possibilities for cancer therapy by enhancing skin permeability and enabling sustained drug release while minimizing systemic side effects. In this study, we developed a multifunctional hydrogel platform by encapsulating varying ratios of ionic liquids (ILs) into the micropores of judiciously selected metal–organic frameworks (MOFs), aiming to improve drug loading and delivery performance. Specifically, we utilized the [TMG][Ol] IL, UiO-66-NH_2 MOF, and carboxymethyl cellulose sodium salt to fabricate a synergistic composite hydrogel. The resulting system demonstrated outstanding thermal stability, mechanical strength, adhesiveness, self-healing properties, and spreadability—key attributes for efficient TDDS applications. Biocompatibility assessments using HaCaT cells showed ~90% cell viability, confirming its cytocompatibility. Composite hydrogels prepared with [TMG][Ol]@UiO-66-NH_2 at ratios of 0.1 : 1 (G1) and 0.25 : 1 (G2) exhibited high drug-loading capacities of 671 mM and 397.8 mM for 5-fluorouracil (5-FU), respectively. *In vitro* transdermal drug penetration over 48 hours reached 76.4% for G1 and 82.7% for G2. Furthermore, cytotoxicity studies on A431 (epidermoid carcinoma) and MCF-7 (breast cancer) cancer cell lines confirmed the therapeutic potential of the drug-loaded hydrogels. Overall, the biocompatible [TMG][Ol]@UiO-66-NH_2-based hydrogel system offers a promising strategy for the transdermal delivery of hydrophilic anticancer agents, supporting its potential for future clinical translation in cancer therapy.

Received 21st April 2025,
Accepted 31st October 2025

DOI: 10.1039/d5tb00931f

rsc.li/materials-b

1. Introduction

Over the past few years, there has been a surge of interest in noninvasive drug delivery methods, leading to significant attention on transdermal and topical drug delivery systems (TDDSs) as promising alternatives to traditional routes like oral consumption or injections.[1] Advantages include avoiding enzymatic degradation, minimizing metabolic burden on the liver and diaphragm, extending therapeutic existence, and improving the response of patients to drugs.[2] The skin serves as an appealing route for transdermal drug delivery (TDD) due to its ease of access and large surface area accessible for drug absorption. At the same time, the skin also serves as a considerable barrier to drug penetration, especially for high-molecular-weight (>500 Da) and hydrophilic molecules ($\log P < 0$).[3] To alleviate this limitation, numerous solutions have been proposed, including physical methods like microneedles or electroporation ablation to reduce barriers and chemical compounds that promote permeability.[4] Chemical permeation enhancers (CPEs), including propylene glycols, sulfoxide, Tween 80, ethanol and menthol derivatives, are commonly used to improve drug penetration; however, they can be hazardous and irritate the skin.[5] To overcome these challenges, fatty acid-based permeation enhancers have been investigated more recently due to their low toxicity and minimal skin irritation.[6] In addition, the limited to no solubility of drugs, particularly hydrophobic anticancer drugs, in pharmaceutically approved solvents also hampers their applications as TDDSs.[7] Ionic liquids (ILs) with their tunable nature and wide range of polarity offer tremendous potential for addressing all of these limitations associated with the conventional drug delivery routes.[8]

A number of attempts were made in the earlier studies to formulate IL-based TDDSs in different forms, such as lipid bilayers, emulsion-based systems, and micelles, to mention a

[a] Ionic Liquids Research Laboratory, Department of Chemistry, Sardar Vallabhbhai National Institute of Technology, Surat-395007, Gujarat, India. E-mail: navedmalek@chem.svnit.ac.in
[b] Analytical Chemistry Division, Bhabha Atomic Research Centre, Trombay, Mumbai-400085, India
[c] Chemistry Department, Faculty of Science, King Khalid University, P.O. Box 9004, Abha 61413, Saudi Arabia

few.[9] In earlier studies, hydrophobic ILs were synthesized using imidazolium as the cation and various anions, such as hexafluorophosphate and tetrafluoroborate, which proved to be effective skin permeation enhancers. The lack of substantial biodegradability, questionable biocompatibility and limited encapsulation efficiencies as well as stability exhibited by these second-generation ILs[10] are addressed by using recently developed fourth-generation biocompatible fatty acid-based ILs (FAB-ILs) as TDDSs in the form of microemulsions, vesicles,[11,12] ionogels[13] and hybrid hydrogels,[14] improving both the skin permeation and solubility of drugs.[15] Furthermore, integrating these FAB-ILs with recently developed metal–organic frameworks (MOFs) will improve not only the drug loading efficiencies but also the stability of the hydrogel while providing controlled release properties.[15] Here, the FAB-ILs are immobilized within the pores of the porous support of MOFs integrating the advantages of both.[16] MOFs, a class of porous materials with high surface areas and tunable compositions, offer a promising support for ILs.[17] Loading ILs onto MOFs with porous structures to form IL@MOF nanohybrids provides them with promising capabilities as drug carriers.[18] Embedding the DOX drug and microwave (MW)-sensitive [Bmim][PF_6] ILs within the pores of ZIF-8 produced ZIF-8/DOX@ZrO_2@IL nanohybrids, designed for therapeutic applications against tumors.[19] Li *et al.* reported that MW-sensitive ILs were loaded onto MIL-101(Fe) to prepare IL@MIL-101(Fe) nanohybrids designed for microwave ablation of tumors.[20]

Among MOFs, zirconium-based MOFs have shown exceptional biocompatibility, biodegradability, and chemical and thermal stability.[21] Amine-functionalized zirconium-based dicarboxylate MOFs, UiO-66-NH_2, have been extensively explored as nanocarriers for the encapsulation and controlled release of drug molecules.[22] The NH_2 functional group strengthens the interaction between drug molecules and MOFs, leading to improved drug binding, loading and controlled release properties.[23] In TDDSs, the duration of skin contact is essential for enhancing drug penetration, thereby increasing the need for adhesiveness, self-healing ability and mechanical stability.[24]

In the pursuit of developing smart TDDSs, in this study, we have designed hydrogels with exceptional biocompatibility, adhesiveness, mechanical properties, drug encapsulation capacity, responsiveness to external stimuli and the ability to penetrate the SC layer of the skin for drug delivery as an ideal solution for next-generation TDDSs. The IL used in this study consists of 1,1,3,3-tetramethylguanidine as the cation and oleic acid as the anion, and is represented as [TMG][Ol]. We used the UiO-66-NH_2 MOF, as MOFs composed of carboxylate linkers and cationic zirconium clusters exhibit excellent potential as drug carriers due to their outstanding aqueous stability, high surface areas and significant loading capacity.[25] We have designed an IL@MOF-based polymeric hydrogel by incorporating [TMG][Ol]@UiO-66-NH_2 into a carboxymethyl cellulose sodium salt-based matrix. The prepared hydrogel was employed to investigate the transdermal delivery of the anticancer drug 5-fluorouracil (5-FU), addressing the selective permeability of skin and the polarity of the drug to facilitate its targeted delivery to infected cells while reducing potential side effects. This unique combination of the IL@MOF composite and biopolymer holds great promise for TDDS applications, as the hydrogel can load drugs such as 5-FU, offering a wide range of possibilities in transdermal drug delivery.

2. Experimental work

2.1. Materials

1,1,3,3-Tetramethylguanidine (TMG), carboxymethyl cellulose sodium salt (CMC-Na), and PBS 7.0 and 5.2 buffer capsules were purchased from Sigma-Aldrich. Zirconium chloride (>98.0%), 2-aminoterephthalic acid and 5-fluorouracil (5-FU) were obtained from TCI (Tokyo Chemical Industry, Japan). Oleic acid was bought from SRL (Sisco Research Laboratory, India). The listed chemicals and reagents had purities over 99% and were of analytical grade; they were used as received without further purification. Double-distilled deionized water was used throughout all experiments.

2.2. Preparation of the [TMG][Ol]@UiO-66-NH_2 composite

The synthesis procedures for pure [TMG][Ol] and pristine UiO-66-NH_2 are provided in the SI. The IL@MOF composites were prepared using the previously described wet impregnation method with minor modifications (Scheme 1).[26] UiO-66-NH_2, in its purest form, was activated by heating at 120 °C overnight under vacuum before incorporating [TMG][Ol]. IL@MOF composites were prepared with varying IL ratios, ensuring that each was loaded to the maximum achievable level without causing mud formation after solvent removal. Accordingly, 20 and 50 mg of [TMG][Ol] were initially dissolved in 20 ml of ethanol with stirring for 1 hour at room temperature, as ethanol was used to dissolve the amino-functionalized basic IL.[27] Then, 200 mg of dehydrated UiO-66-NH_2 powder was added to the solution to prepare [TMG][Ol]@UiO-66-NH_2 with ratios of 0.1 : 1 and 0.25 : 1. After the solvent was evaporated by stirring the mixture at 35 °C in open air, the resulting composites were dried overnight in an oven at 60 °C.

2.3. Preparation of the hydrogel

To prepare the hydrogel (Scheme 1), a suspension of IL@MOF composites in deionized water was initially prepared. In brief, 2% w/v of the [TMG][Ol]@UiO-66-NH_2 composite was added to deionized water and thoroughly mixed using a magnetic stirrer to ensure even dispersion of the composite throughout the water. Ultrasonication was conducted for 30 minutes to improve the dispersion of particles. Following the addition of 2% CMC-Na, the mixture was heated to 35 °C under stirring with a magnetic stirrer until CMC-Na was completely dissolved, resulting in hydrogel formation. The components utilized in this experiment for preparing the composites and hydrogels are shown in Table 1.

2.4 Characterization of IL@MOF composites and hydrogels

Using the Brunauer–Emmett–Teller (BET) equation, the surface area and pore volume of the pristine MOFs and their IL@MOF

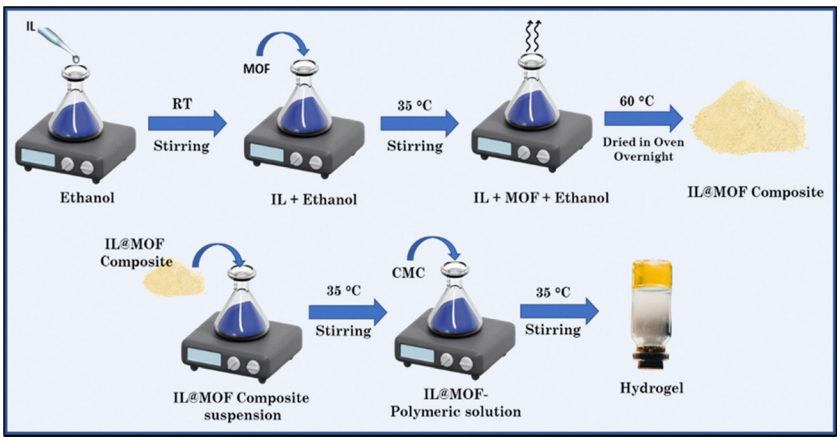

Scheme 1 Schematic representation of the preparation of the IL@MOF composites and hydrogels.

Table 1 Composition used in the formation of hydrogels in the current study

Abbreviation	Molar ratio ([TMG][Ol]@UiO-66-NH_2)	IL@MOF composite (%)	CMC-Na (%)	Remarks
[TMG][Ol]@UiO-66-NH_2 (0.1 : 1)	0.1 : 1	2	—	Powder
[TMG][Ol]@UiO-66-NH_2 (0.25 : 1)	0.25 : 1	2	—	Powder
[TMG][Ol]@UiO-66-NH_2 (0.1 : 1)	0.1 : 1	2	1	Viscous solution
[TMG][Ol]@UiO-66-NH_2 (0.25 : 1)	0.25 : 1	2	1	Viscous solution
G1	0.1 : 1	2	2	Gel
G2	0.25 : 1	2	2	Gel

composites were calculated using N_2 adsorption isotherms at 77.35 K. X-ray photoelectron spectroscopy (XPS) measurements were performed using a Thermo Scientific NEXA surface analyzer to analyze the chemical composition within the range of 0 to 1350 eV. An X-ray diffractometer with monochromatic Cu-Kα (1.54056) radiation (40 kV, 30 mA) was used to record the X-ray diffraction (XRD) patterns. The diffractometer was operated in the 2θ range of 5–60° at a rate of 3° per minute. The Fourier transform infrared (FT-IR) spectra of [TMG][Ol], UiO-66-NH_2, [TMG][Ol]@UiO-66-NH_2 composites, CMC-Na and the prepared [TMG][Ol]@UiO-66-NH_2-based hydrogel were recorded using a Jasco 6000 spectrophotometer to identify potential interactions responsible for gel formation. Small-angle neutron scattering (SANS) investigations were carried out at the Guide Tube Laboratory, Dhruva Reactor, Bhabha Atomic Research Centre, Mumbai, India using a SANS-I diffractometer. We used SasView analytic software to investigate the experimental scattering data using a variety of fitting models. The thermal stability and decomposition characteristics of UiO-66-NH_2, [TMG][Ol], [TMG][Ol]@UiO-66-NH_2 composites, and the [TMG][Ol]@UiO-66-NH_2-based hydrogel were analyzed using thermogravimetric analysis (TGA). The samples were examined using SDT Q600 V20.9 Build 20 TGA apparatus, which was heated from 25 to 800 °C in an aluminum pan at a rate of 10 °C per minute with a nitrogen flow at 100 mL min^{-1}. To assess the thermal behavior, DSC analysis was conducted by cycling the temperature from 25 °C to 250 °C and back to 25 °C at a constant heating and cooling rate of 10 °C min^{-1}. FE-SEM images of the UiO-66-NH_2, [TMG][Ol]@UiO-66-NH_2 composites, [TMG][Ol]@UiO-66-NH_2-based hydrogel and drug-loaded hydrogel were captured using a QUANTA 200 FESEM.

2.5. Mechanical property evaluation using rheology

The properties of the hydrogels were examined using an Anton Paar Physica MCR 301 rheometer to analyze their mechanical properties. We used a parallel plate configuration with a 40 mm diameter and 0.5 mm spacing, with an attached transducer. Measurement of angular frequency sweep was performed over the range of 1–100 rad s^{-1}, while keeping a constant strain of 1%, to assess the rheological properties. At a constant frequency of 1 rad s^{-1} and with strain against modulus of G' and G'' of 0–1%, the strain sweep analysis was performed. The viscosity of the hydrogels was measured at shear rates ranging from 0 to 100 (1/s).

Two glass slides (6 cm) of standard size were used to evaluate spreadability while accounting for the ''slip'' and ''drag'' characteristics of the gel. After applying 2 g of the hydrogel to one slide, a second slide was placed on top of the gel, sandwiching it between the two slides. The excess gel was scraped off from the edges. The time (s) required for the top slide to move 6 cm was noted. This time interval reflects the gel's spreadability. Spreadability was calculated using eqn (1):

$$S = \frac{M \times L}{T} \quad (1)$$

where S stands for spreadability, M for the weight, L for the glass slide length moved, and T for time.

2.6. Drug loading study within the hydrogel

We used the swelling equilibrium approach, a reliable method, to load the 5-FU drug (hydrophilic drug) into the prepared hydrogel. Before use, 17.5 mm dialysis membranes were immersed in distilled water overnight. A precisely measured amount of the hydrogel was then carefully placed into the dialysis membrane. For 24 hours at room temperature, this assembly was then immersed in a predefined concentration of drug solution. The evaluation of the drug loading capacity in the hydrogel was carried out using drug absorption measurements. Using a standard calibration curve, we ascertained the loaded drug (5-FU) concentration in the gel.

2.7. *In vitro* drug permeation studies

A Franz diffusion cell was used for skin penetration experiments as mentioned previously.[28] After carefully removing the fat layer, the skin was sliced into 1.5 × 1.5 cm^2 pieces. After that, these skin pieces were placed in a Franz diffusion cell, which contained 10 mL of phosphate buffered saline and was continuously shaken at 32 ± 1 °C, with the inner skin facing the receptor phase. The donor compartment, on the exterior side of the skin, was then covered with 0.5 g of the 5-FU-loaded hydrogel and protected with parafilm to avoid contamination. 0.25 mL samples were taken out of the receiving chamber at regular intervals over a period of 48 hours and these samples were examined using UV-vis spectroscopy to measure the amount of 5-FU released at various intervals.

2.8. Stratum corneum (SC) study using FT-IR

The goat skin was taken out of the freezer and allowed to thaw for an hour at room temperature. After the top layer was removed, the goat skin was submerged in a trypsin solution and floated overnight to separate any dermal tissues from the SC. The SC was washed with PBS and then allowed to dry at room temperature for 72 hours. After obtaining the control sample, the FT-IR spectrum of a 0.5 cm × 0.5 cm sample of goat skin SC was recorded. Here, the sample was incubated with the examined material for a duration of 24 hours. The next day, the sample was washed with PBS and allowed to air-dry for 72 hours, and the FT-IR spectrum of the SC of goat skin was measured again. This second spectrum was compared with the spectrum of the untreated SC to determine the impact of the test substance on the SC structure.

2.9. *In vitro* biocompatibility and cytotoxicity assays

The biocompatibility of the system was tested *in vitro* using the MTT (3-(4,5-dimethylthiazol-2-yl)-2,5-diphenyltetrazolium bromide) assay. A human keratinocyte cell line (HaCaT) was used in the experiment. The cells (10 000 cells per well) were grown in a 96-well plate for 24 hours in DMEM supplemented with 1% antibiotic solution and 10% FBS at 37 °C with 5% CO_2. Hydrogels at various concentrations were added into cell-filled wells for 48 hours. Cell viability was measured using the MTT assay, and each concentration of the hydrogel was compared to the positive control (without hydrogel). The same procedure was applied to assess the cytotoxicity of the anticancer drug (5-FU)-loaded hydrogels in human epidermoid carcinoma (A431) and breast cancer (MCF-7) cell lines, with the aim of determining drug efficacy and IC_{50} values.

3. Results and discussion

Integrating a judiciously designed biocompatible IL within the MOF can transform the IL@MOF composite by enhancing its stability, tunability, and functional properties. The IL plays a crucial role in modifying surface chemistry, improving guest molecule interactions, enhancing drug permeation and facilitating controlled drug release, making the system highly efficient for biomedical applications. However, the addition of excessive ILs causes the MOF (powder form) to become viscous and muddy, resulting in greater experimental uncertainties and also pore blockage within the MOFs.[29] Herein, we primarily investigate and analyze the encapsulation of two [TMG][Ol] proportions (0.1 and 0.25) within the micropores of UiO-66-NH_2 to form [TMG][Ol]@UiO-66-NH_2 (0.1 : 1) and [TMG][Ol]@UiO-66-NH_2 (0.25 : 1).

The successful encapsulation of [TMG][Ol] within the microporous structure of UiO-66-NH_2 was demonstrated using N_2 adsorption/desorption tests (Fig. 1A). With increasing the concentration of [TMG][Ol], the overall specific surface area decreases (Table 2).[27,30] The calculated BET surface areas of the prepared UiO-66-NH_2, [TMG][Ol]@UiO-66-NH_2 (0.1 : 1) and [TMG][Ol]@UiO-66-NH_2 (0.25 : 1) were 272.83 $m^2\ g^{-1}$, 100.37 $m^2\ g^{-1}$, and 5.62 $m^2\ g^{-1}$, respectively, which are notably higher than those reported for $[PP_{13}][TFSI]$@NH_2-MIL-53(Al).[31] As the IL content in the UiO-66-NH_2 powder increased, a corresponding increase in particle size was also observed, further confirming the successful encapsulation of [TMG][Ol] into the nano–micropores of UiO-66-NH_2.

The elemental compositions and electronic interactions in the prepared materials were further examined using XPS analysis. The XPS spectra of UiO-66-NH_2, both the IL@MOF composites and both the IL@MOF composite hydrogels contain clear peaks associated with C 1s, N 1s, O 1s and Zr 3d electrons (Fig. 1B). We confirmed the coexistence of Zr, C, N and O element peaks at 182.2, 284, 399.1 and 531.5 eV in all materials. Additionally, the binding energy peaks observed at 1071 and 497 eV in the spectra of both the hydrogels (G1 and G2) can be attributed to sodium (Na 1s at 1071 eV and Auger peaks at 497 eV), resulting from the addition of carboxymethyl cellulose sodium salt to prepare the hydrogel. The XPS atomic content data, shown in Table S1, indicate an increase in nitrogen atom content in [TMG][Ol]@UiO-66-NH_2 composites, attributed to the presence of the amine group in [TMG][Ol].

The high-resolution Zr 3d XPS spectrum shows peaks at 185.44 and 183.07 eV, corresponding to Zr^{4+} $3d_{3/2}$ and $3d_{5/2}$ energy levels (Fig. 1C) in UiO-66-NH_2 and [TMG][Ol]@UiO-66-NH_2-based composites.[33] These peaks shift to higher binding energies compared to those corresponding to UiO-66-NH_2 in the hydrogel samples. In the C 1s XPS spectra of UiO-66-NH_2

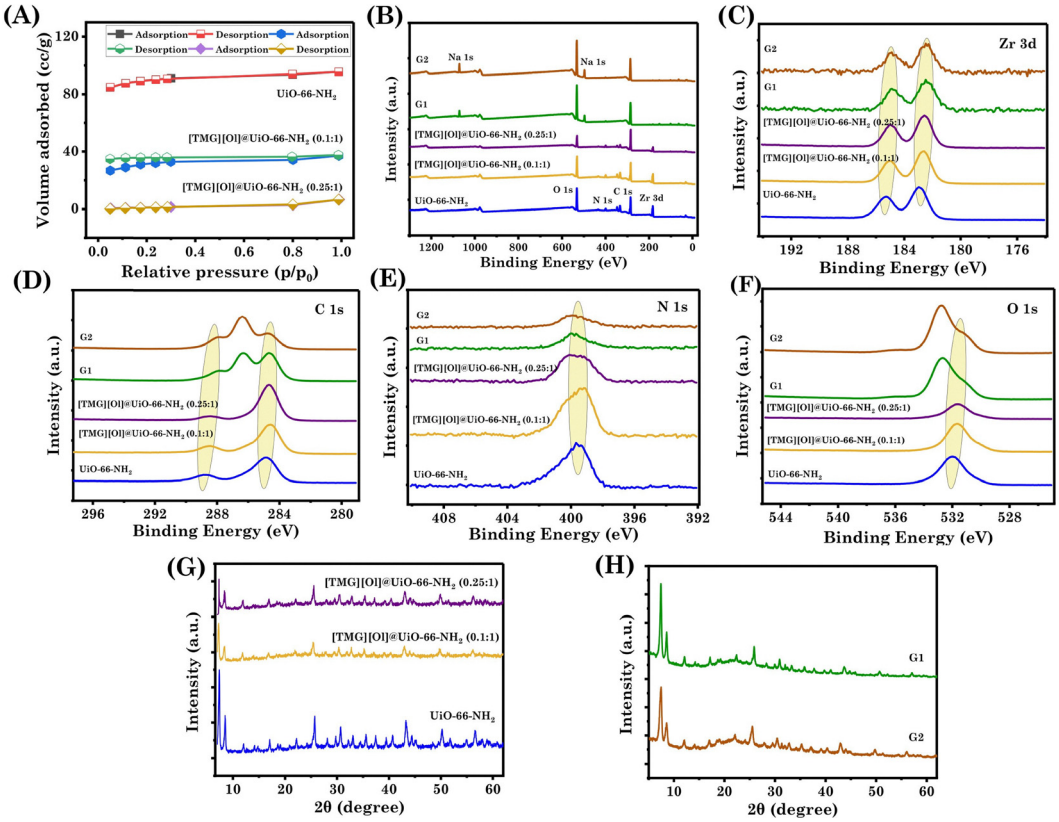

Fig. 1 (A) N_2 adsorption–desorption isotherms of UiO-66-NH_2 and UiO-66-NH_2-IL composites; (B) wide-scan XPS spectra; high-resolution XPS spectra of (C) Zr 3d, (D) C 1s, (E) N 1s, and (F) O 1s; PXRD patterns of (G) MOF and IL@MOF composites and (H) IL@MOF composite-based hydrogels.

Table 2 Total specific surface area, pore volume and pore radius for N_2 adsorption/desorption of different ratios of ILs

Sample	Surface area ($m^2\ g^{-1}$)	V_{total} ($cc\ g^{-1}$)	Pore radius (Å)
UiO-66-NH_2	272.83	0.15	<933.4
[TMG][Ol]@UiO-66-NH_2 (0.1 : 1)	100.37	0.057	<953.3
[TMG][Ol]@UiO-66-NH_2 (0.25 : 1)	5.62	0.010	<1108.8

and [TMG][Ol]@UiO-66-NH_2-based composites, we observed two distinct peaks at 288.7 (C═O) and 284.8 eV (C–C, C═C, C–H). However, when characterizing the hydrogel samples, *i.e.* in G1 and G2, we observed an additional peak at 286.3 eV, which may be associated with the carbon in C–O and C–O–C groups (Fig. 1D).[32] The N 1s spectrum displays a peak at 399.4 eV, attributed to the nitrogen in the –NH_2 group (Fig. 1E).[33] The O 1s spectra of UiO-66-NH_2 and both the IL@MOF composites show a single peak at 531.6 eV, while in the G1 and G2 hydrogels, two distinct peaks are observed at 531.6 and 532.7 eV, corresponding to the oxygen in C═O and C–O (O–C–O and C–OH), respectively (Fig. 1F).[34] In all the spectra discussed above, a slight shift to lower binding energies is observed, indicating a strong interaction between UiO-66-NH_2 and [TMG][Ol], as well as between the [TMG][Ol]@UiO-66-NH_2 composite and CMC-Na.

The crystalline nature of the synthesized UiO-66-NH_2 and its modifications with the IL was examined using XRD analysis (Fig. 1G). The pristine UiO-66-NH_2 exhibited characteristic diffraction peaks corresponding to its well-defined crystalline framework, confirming the successful synthesis of a highly ordered porous structure. Sharp diffraction peaks at 2θ = 7.5° and 8.5°, corresponding to the (111) and (002) planes, further indicated the formation of pure UiO-66-NH_2 MOF nanoparticles.[35] Modification with [TMG][Ol] decreases the intensity, but the integrity is not greatly affected. However, the retention of diffraction peaks suggested that the structural integrity of UiO-66-NH_2 was largely preserved. The formation of the IL@MOF-based hydrogel further altered the diffraction pattern, showing the broadening of peaks, which can be attributed to the amorphous nature of the polymeric network and the dispersion of [TMG][Ol]@UiO-66-NH_2 within the hydrogel matrix (Fig. 1H). With an increase in [TMG][Ol] concentration in the composites ([TMG][Ol]@UiO-66-NH_2 (0.25 : 1)) and the hydrogel (G2), the peak intensity decreased further, indicating a gradual loss of crystallinity. This reduction can be attributed to the disruption of the long-range order of UiO-66-NH_2 due to [TMG][Ol] incorporation, which may lead to partial pore filling, or interactions between [TMG][Ol] and UiO-66-NH_2, thereby affecting its structural integrity.

Building on the prior study, the FT-IR spectra were used to analyze the chemical interactions and functional groups within the material (Fig. 2A). In the spectra of [TMG][Ol], a broad band at 3350–3290 cm^{-1} corresponds to N–H stretching, which

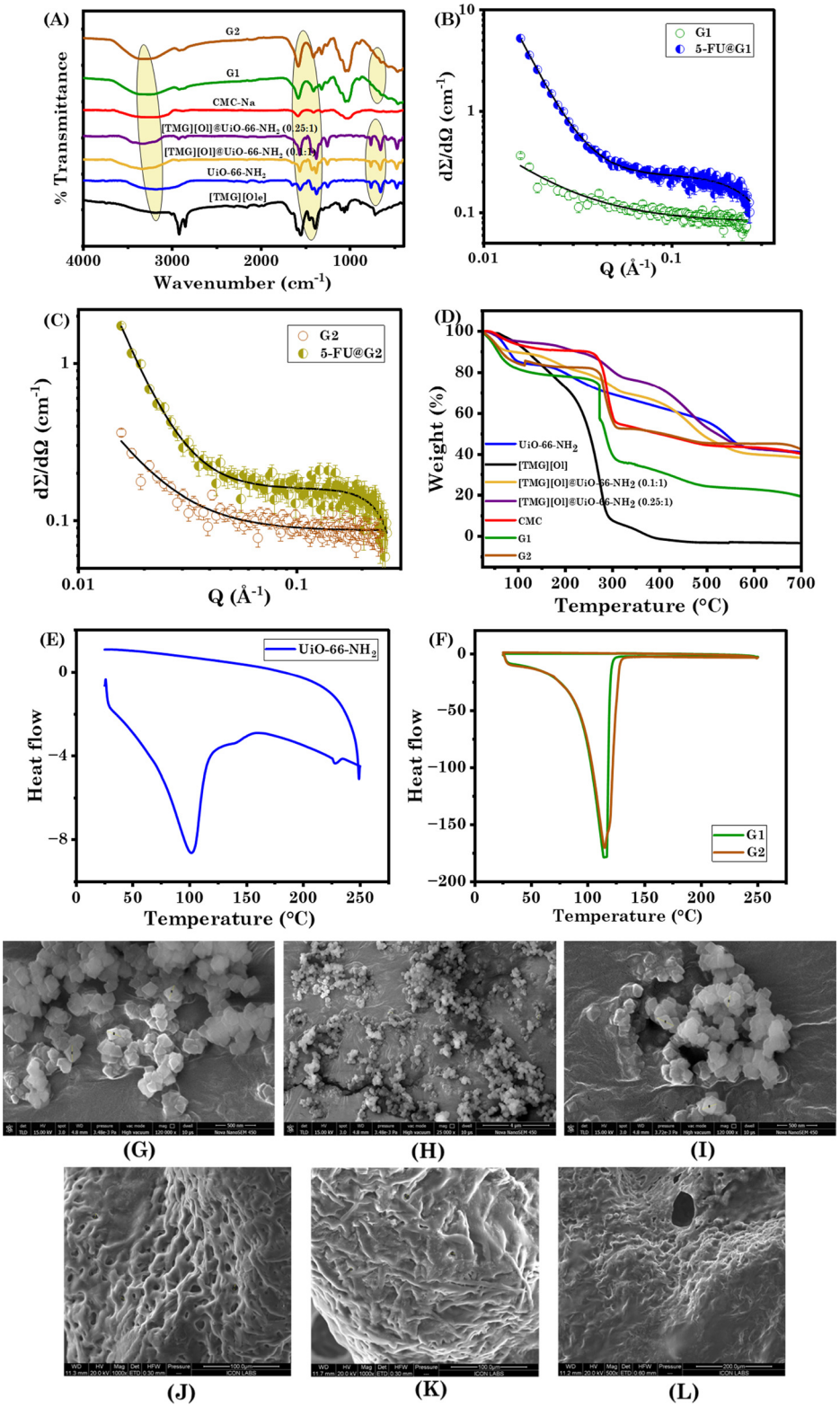

Fig. 2 (A) FT-IR spectra of pure components and the prepared composites and hydrogels; SANS graphs of (B) G1 and 5-FU@G1 and (C) G2 and 5-FU@G2. (D) TGA curves of the MOF, IL, IL@MOF composites and hydrogel; DSC curves of (E) UiO-66-NH_2 and (F) G1 and G2; FE-SEM images of (G) UiO-66-NH_2, (H) [TMG][Ol]@UiO-66-NH_2 (0.1 : 1), (I) [TMG][Ol]@UiO-66-NH_2 (0.25 : 1), (J) G1, (K) G2, and (L) 5-FU@G1.

validates the existence of the C=NH_2^+ cationic group. Olefinic C–H stretching in ILs occurs at about 3005 cm^{-1}. Sharp peaks at 2925–2850 cm^{-1} suggest the C–H stretching of methyl and methylene units. Two bands—symmetric stretching at

1441–1401 cm^{-1} and asymmetric stretching at 1598–1553 cm^{-1}—confirm the carboxylate anion. C═C stretching combined with C═N is observed at around 1655 cm^{-1}; from these findings, the successful synthesis of [TMG][Ol] is confirmed.[36] As for UiO-66-NH_2, broad peaks at 3450 and 3250 cm^{-1} confirm the presence of the N–H bond of the amino group in 2-aminoterephthalic acid. At 1259 cm^{-1}, the peak indicates the C–N bonds of aromatic amines. Characteristic bands were assigned to the carboxyl group from 2-aminoterephthalic acid at 1375 cm^{-1}, 1426 cm^{-1}, and 1561 cm^{-1}. The Zr–O bond is responsible for the absorption bands at 763 and 685 cm^{-1}, and all of the distinctive peaks observed were consistent with those reported in the literature.[37]

For the composite, a blue shift from 3203 cm^{-1} to 3343 cm^{-1} was observed, likely caused by strong hydrogen bonding or electrostatic interactions between the –NH_2 groups of UiO-66-NH_2 and $[Ol]^-$ in [TMG][Ol]. Broadening in the N–H stretching region (around 3200 cm^{-1}) indicates hydrogen bonding between $[TMG]^+$ and the –NH_2 groups of MOFs. A slight shift of the carboxylate –C═O stretching band of the MOF in the composite can indicate strong interactions with [TMG][Ol].

To analyze hydrogel formation, we compared the spectra of the hydrogels with those of their IL@MOF composites and the gelator. In both G1 and G2 hydrogels, shifts in the –OH and –CO peaks indicate strong hydrogen bonding interactions between the [TMG][Ol]@UiO-66-NH_2 composites and CMC-Na. The spectra of the hydrogels closely resemble those of the IL@MOF composites, with an additional new peak at 1027 cm^{-1} attributed to the C–O–C bond of CMC-Na, while the N–H band from UiO-66-NH_2 merges with the O–H band. The Zr–O bonds observed at 763 and 685 cm^{-1} in both the [TMG][Ol]@UiO-66-NH_2 composites and the hydrogels (G1 and G2) confirm the stability and intact presence of the UiO-66-NH_2 structure.

Furthermore, SANS analysis was carried out on the hydrogel samples before and after drug loading to investigate the internal structure and to understand the structural changes induced by drug incorporation. For the G1 and G2 hydrogels, the scattering data were well-fitted using the mass fractal model, indicating a self-similar, loosely connected network structure (Fig. 2B). $S(Q)$ in the context of mass fractal structures may be obtained using eqn (2):

$$S_{mf}(Q) = 1 + \frac{1}{(QR_b)^{D_m}} \frac{D_m \Gamma(D_m - 1)}{[1 + (Q\xi)^{-2}]^{\frac{(D_m-1)}{2}}} \times \sin\{(D_m - 1) \times \tan^{-1}(Q\xi)\}, \quad (2)$$

where ξ signifies the maximum length up to which the fractal microstructure exists, R_b denotes the building block size and D_m is the mass fractal dimension.

In the G2 hydrogel, a decrease in the building block radius along with an increase in the fractal dimension was observed, suggesting a transition toward a more compact and densely cross-linked network, likely due to an increase in [TMG][Ol] concentration that enhances molecular interactions and network tightening as shown in Table 3. The parameter D_m serves as a measure of the openness of fractal structures, where a value of 1 indicates loosely connected aggregates, and a value of 3 corresponds to densely packed aggregates.[38] However, the scattering profiles of the drug-loaded hydrogels were better fitted with the correlation length model,[39] indicating the presence of short-range structural correlations rather than a fractal-like arrangement.

Table 3 Fitting parameters of hydrogels before and after drug loading

Before drug loading	Building block radius (Å)	Fractal dimension (D_m)	Model
G1	5.93	1.52	Mass fractal
G2	5.10	2.15	Mass fractal
After drug loading	**Correlation length (Å)**	**Power coefficient**	
5-FU@G1	2.98	3.68	Correlation length
5-FU@G2	1.82	3.45	Correlation length

$$I(Q) = \frac{A}{Q_m} + \frac{C}{(1 + Q\xi^m)} + B. \quad (3)$$

The Porod function, the first component in this formula, characterizes the clustering of the gel structure at large length scales. The incoherent background is B, and the Porod exponent m describes the hydrogel's fractal aspect. The second term is the Lorentzian function; in particular, the Lorentzian exponent is the inverse of the Flory exponent, and the correlation length of the polymer chains is represented by ξ. This change in the fitting model indicates that drug encapsulation induces a structural reorganization within the gel matrix (Fig. 2C). The corresponding fitting parameters are presented in Table 3.

The thermal stability of the synthesized [TMG][Ol], UiO-66-NH_2, [TMG][Ol]@UiO-66-NH_2 composites and hydrogels was evaluated using TGA. As shown in Fig. 2D, three phases of weight loss are observed in pure UiO-66-NH_2. The evaporation of absorbed water is the reason for the first weight loss, which occurs between 50 and 100 °C. The second weight loss then occurs in the 160–260 °C range due to the loss of the remaining DMF molecules in the MOF. It exhibits a gradual degradation phase between 300 and 550 °C. After that, MOF crystallinity is lost as the MOF breaks down into tetragonal zirconia.[40,41] In [TMG][Ol], a gradual mass loss was observed between 60 °C and 200 °C, followed by a sharp decline, with the material remaining stable up to 300 °C. The TGA of the [TMG][Ol]@UiO-66-NH_2 composites revealed a mass loss pattern similar to that of pristine UiO-66-NH_2, indicating comparable thermal behavior with distinct variations due to the incorporation of [TMG][Ol]. The weight loss of both composites is primarily attributed to the evaporation of solvent molecules. We observed that the [TMG][Ol]@UiO-66-NH_2 composite exhibited greater thermal stability compared to both the pristine [TMG][Ol] and UiO-66-NH_2 (Fig. 2D). In the IL@MOF composite hydrogel, the initial weight loss up to 100 °C is primarily due to the evaporation of water. The hydrogel remained stable up to 300 °C, after

which a sharp mass loss was observed, attributed to the degradation of CMC-Na.[42] Overall, the IL@MOF-based hydrogel demonstrates enhanced thermal stability compared to its pristine form.

The remarkable thermal stability of both UiO-66-NH_2 (Fig. 2E) and the hydrogels (Fig. 2F) was further confirmed by DSC analysis. The DSC thermograms exhibited no significant endothermic or exothermic transitions up to 100 °C, indicating the absence of any thermal degradation or phase transitions within this temperature range. These results corroborate the TGA findings and further establish the thermal robustness of the developed system for drug delivery applications.

Furthermore, the surface morphology and microstructural characteristics of the pure MOF, IL-MOF composites, IL@MOF-based hydrogel and drug loaded IL@MOF-based hydrogel were analyzed using FE-SEM. As shown in Fig. 2G, octahedral UiO-66-NH_2 was effectively constructed with regular crystal faces and a relatively uniform dimension with an average size of 188 nm. The morphology of the studied UiO-66-NH_2 is similar to that observed by Zhang *et al.*[43] Even after the incorporation of the IL, *i.e.* [TMG][Ol]@UiO-66-NH_2 (0.1 : 1) and [TMG][Ol]@UiO-66-NH_2 (0.25 : 1), the composites maintained a consistent octahedral shape with average sizes of 212 and 266 nm, respectively (Fig. 2H and I). This finding suggested that the structure of the MOF was preserved during the modification process. Fig. 2J and K shows a highly porous, interconnected network structure characteristic of hydrogels, facilitating drug encapsulation and release. The hydrogel matrix indicated that pores in G1 and G2 gels were uniformly distributed and had average sizes of 6.2 and 5.6 μm, respectively. The hydrogel surface exhibits a rough texture, indicating the incorporation of the [TMG][Ol]@UiO-66-NH_2 composite within the polymer matrix. The incorporation of the IL@MOF composite into the hydrogel is confirmed by the characterization results, which reveal the dispersion of distinct nanocrystals throughout the hydrogel matrix. The drug-loaded hydrogel has a slightly more irregular surface compared to the unloaded hydrogel, which is most likely caused by the interaction of the 5-FU molecules with the [TMG][Ol]@UiO-66-NH_2 composite (Fig. 2L). The pores are distributed, with an average size of 3.5 μm, and the incorporation of 5-FU slightly reduces the overall porosity of the hydrogel compared to the drug-free hydrogel.

Rheological analyses were conducted to evaluate the mechanical strength of the hydrogels, which provided important information about their viscoelastic behavior and mechanical characteristics.[14,44] The mechanical strength of the hydrogels under study was investigated through angular frequency sweep measurements. The analysis revealed variations in the storage moduli (G') and loss moduli (G'') as a function of angular frequency at 25 °C, as depicted in Fig. 3A. The findings show that, for a constant strain of 0.1%, the storage modulus (G') continuously exceeds the loss modulus (G'') throughout a broad frequency range, *i.e.*, up to 100 rad s^{-1}. This phenomenon can be elucidated by the robust colloidal forces present within the gel network.

To determine the viscoelastic behavior of the hydrogels, the strain sweep test was conducted. Crossover points (γ_c) for G1 and G2 hydrogels were observed at 8.3 and 10.8% strain values, respectively, as shown in Fig. 3B. The higher strain values observed in the G2 hydrogel are attributed to the higher concentration of [TMG][Ol] within the hydrogel matrix. The area below γ_c where G' is greater than G'' is referred to as an elastic or a linear region. The hydrogel behaves like a semisolid material in this region. Above γ_c, G' is less than G'', indicating that the hydrogel is distorted and behaves like a viscous solution. The strain sweep data show that the hydrogels exhibit viscoelastic characteristics.

The viscosity study is essential in drug delivery systems to understand hydrogel behavior during treatment. High viscosity can lead to obstructions and difficulties, whereas low viscosity could hinder drug delivery. In this study, we observed a reduction in the viscosity of the hydrogel when increasing the shear rate from 0.1 to 100 s^{-1} (Fig. 3C). The hydrogels flow with increasing shear rate, as evidenced by the steady shear flow (flow curve). At low shear rates, hydrogels exhibit shear-thinning behaviour, maintaining a relatively high viscosity that causes a sharp increase in shear stress. Shear-thinning in the hydrogels indicates decreased viscosity because shear stress increases at a diminishing pace as the shear rate increases (Fig. 3D).

For use as an intelligent TDDS, the hydrogel should exhibit self-healing properties. We used a conventional visual observation technique, in which circular gels were placed close together, to evaluate the self-healing capability of the hydrogel under investigation. The two hydrogel fragments seemed to self-heal after five minutes, forming a single piece (Fig. 3E). This result was confirmed by stretching the hydrogel using a pair of tongs, where it was observed that the hydrogel did not break, particularly in the healed regions. The entire procedure demonstrates that the hydrogel can self-heal without the need for external stimuli.

To achieve optimal therapeutic benefits, it is essential that hydrogels possess good spreadability when applied to the skin or specific target areas. At room temperature, the G1 and G2 hydrogels exhibit average spreadability values of 19.16 ± 0.9 and 20.12 ± 1.1 g cm^{-1} s^{-1}, respectively. These results demonstrate the application and possible therapeutic effects of the hydrogel by adjusting its spreadability.

For TDDSs, adhesive behaviour is crucial because the contact duration of a drug with the skin has a significant influence on drug penetration. Owing to its non-covalent interactions with the substrates, the investigated hydrogel was tested for its capacity to form bonds with a variety of biological systems, including the skin, as well as hard surfaces, including rubber, steel, plastic and glass (Fig. 3F).[13] Functional groups like NH_2, OH and COO^- endow the hydrogel with adhesive properties and are responsible for the noncovalent interactions with other functional groups on the surface of these materials.[45] Underwater adhesiveness is essential for transdermal drug delivery, ensuring extended skin contact and sustained drug release even under moist conditions. This characteristic was assessed by testing the adhesive strength of the hydrogel under aqueous conditions (Fig. 3G). The hydrogel exhibited strong adhesion

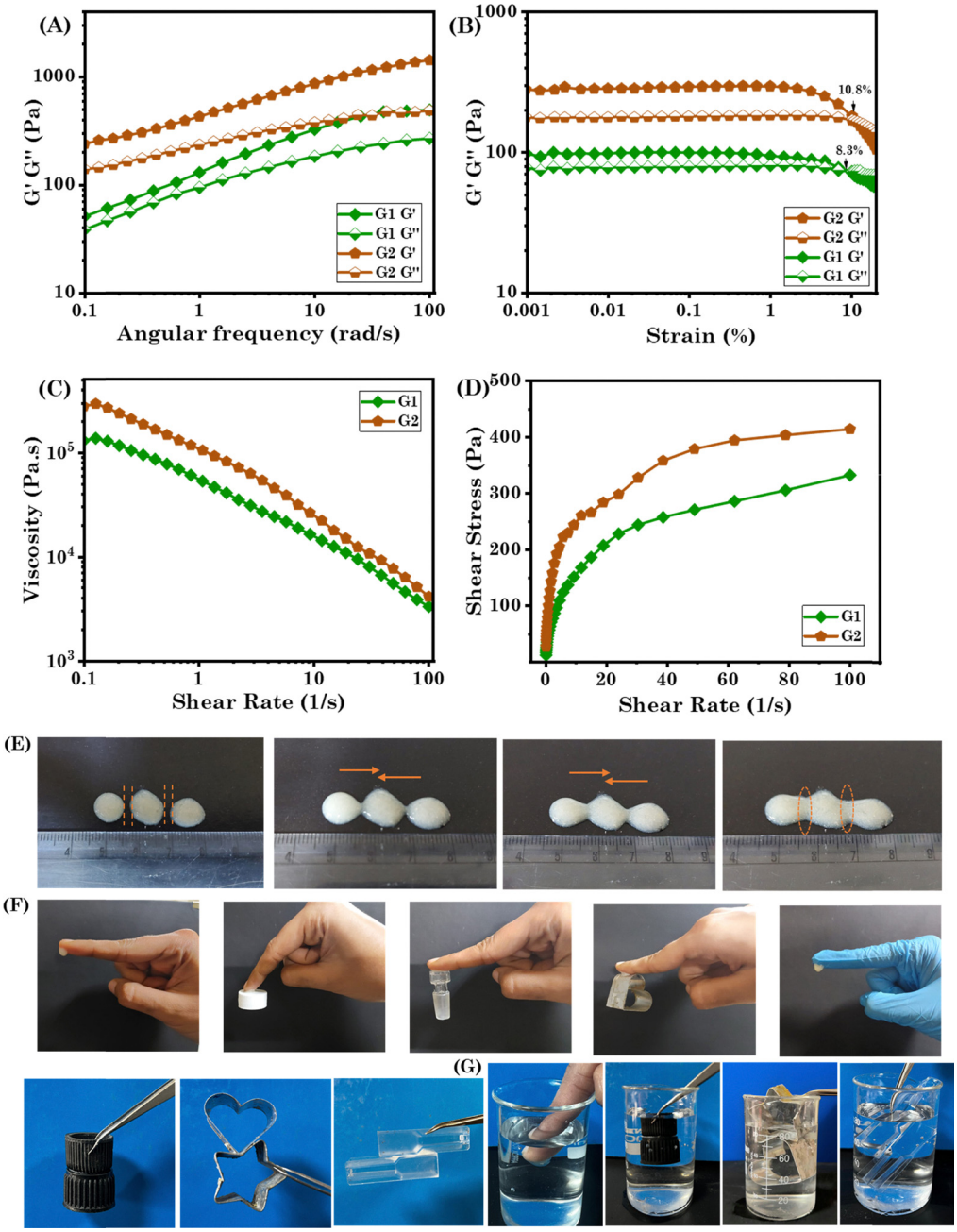

Fig. 3 (A) Frequency sweep data of hydrogels at a constant strain of 0.1%. (B) Strain sweep with a constant frequency of 1 rad s^{-1}. (C) and (D) Viscosity measurement. (E) Visual images showing the self-healing capability of the gel. (F) Adhesive characteristics with skin, rubber, plastic, glass and metal. (G) Adhesive properties in an aqueous environment.

even in the presence of water, indicating that it might be used under physiological conditions in a stable and efficient manner. This feature improves drug penetration and sustains prolonged contact, making it more appropriate for transdermal drug delivery.

3.1 *In vitro* biocompatibility assay with HaCaT cells

Assessing material compatibility is critical for DDSs to ensure safety and efficacy. The biocompatibility of the G1 and G2 hydrogels was evaluated using the HaCaT cell line at a concentration of 1000 μg mL^{-1}, revealing 91.94% and 91.29% cell viability, respectively (Fig. 4A). This noteworthy outcome shows that the hydrogel is highly biocompatible, which is extremely promising for its potential applications in drug delivery and skin tissue engineering. This is attributed to the use of biocompatible materials in the formation of hydrogels, including UiO-66-NH_2, [TMG][Ol], and CMC-Na.[11,46,47] The control image of HaCaT cells is shown in Fig. 4F, and the cell viability after 48 hours of treatment with the IL@MOF-based hydrogel is shown in Fig. 4G and H.

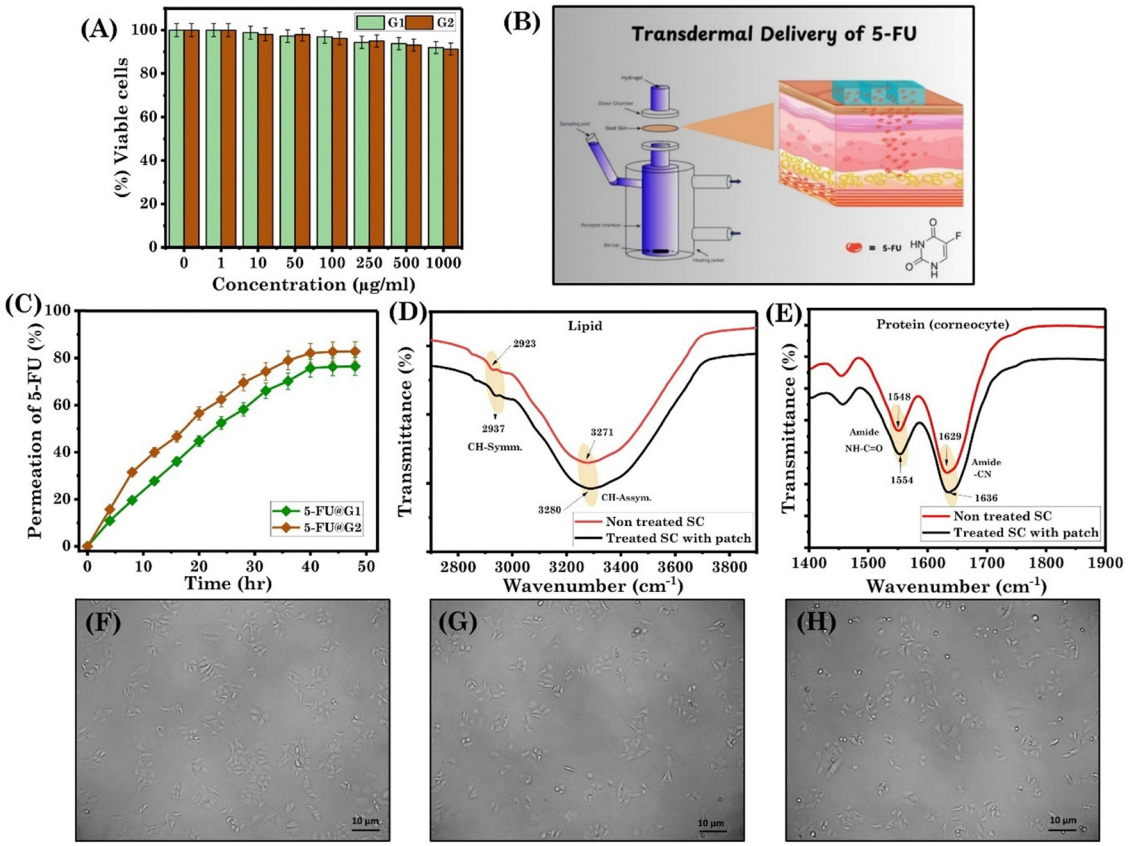

Fig. 4 (A) HaCaT cell viability (%). (B) Schematic representation of transdermal drug delivery using a Franz diffusion cell. (C) Permeation of 5-FU as a function of time at pH 7.4; FT-IR spectrum of the SC before and after treatment with the drug-loaded patch: (D) lipid, (E) protein, (F) HaCaT control and after 48-h treatment with (G) G1 and (H) G2.

3.2 Drug (5-FU) loading profile and *in vitro* permeation study of 5-FU in the hydrogel

Hydrogels have shown great promise in the loading and delivery of anticancer drugs like 5-FU. Hydrogels are ideal for drug administration in cancer treatment and wound healing due to their unique properties, which include their self-healing capacity and adherence to the matrix and skin. In this research, we particularly investigated the capacity of the hydrogels to be loaded with the anticancer drug 5-FU. 5-FU is a robust anticancer drug that interrupts DNA synthesis and limits cancer cell proliferation.[48] The drug loading capacity of 5-FU in G1 and G2 is 671 mM and 397.8 mM, respectively, corresponding to approximately 4-fold and 3-fold increases compared to the hydrogel without [TMG][Ol]@UiO-66-NH_2. This significant enhancement highlights the remarkable drug loading efficiency of the hydrogel. The higher drug loading capacity observed in G1 compared to G2 can be attributed to the greater surface area and pore volume of the [TMG][Ol]@UiO-66-NH_2 (0.1 : 1) composite used in G1. In contrast, the increased [TMG][Ol] content in G2 likely caused pore blockage within the UiO-66-NH_2 structure, thereby limiting the available sites for drug encapsulation. Furthermore, the enhancement of solubility is also attributed to the presence of non-covalent interactions, *i.e.*, hydrogen bonding, electrostatic interactions, π–π stacking, steric interactions and pore confinement.

For successful penetration through the skin, drug molecules should pass through the SC barrier.[49] Drugs must have a molecular weight of less than 500 Da, considerable lipophilicity (a log octanol–water partition coefficient between 1 and 3), and a melting point of less than 200 °C in order to pass through the skin.[50] 5-FU has a log octanol–water coefficient of −0.89, which makes penetration challenging;[51] this problem is addressed by encapsulating 5-FU in hydrogels. Using goat skin, we examined the *in vitro* skin penetration of 5-FU through the Franz diffusion cell at 32 °C over 48 hours (Fig. 4B). Goat skin is used because its biological properties are similar to those of human skin.[52] Under normal physiological conditions (pH 7.4), the 5-FU permeation percentages for 5-FU@G1 and 5-FU@G2 hydrogels are found to be 76.4% and 82.7%, respectively (Fig. 4C). As oleic acid serves as a penetration enhancer in both systems, they exhibit high permeation of 5-FU through the skin. However, since the [TMG][Ol] concentration is higher in 5-FU@G2, we observed greater permeation. In general, the majority of fatty acids have a good ability to improve skin penetration.[53] There is one unsaturation in oleic acid in the form of a π-bond, which may form π–π interactions with the SC layer, improving drug penetration through the skin.[54] Both hydrogels exhibited these interactions, which led to better skin penetration as compared to conventional skin penetration enhancers like Tween-80 and

other CPEs.[55] These results imply that hydrogels based on [TMG][Ol]@UiO-66-NH_2 have the potential to deliver drugs through the skin.

In TDD, the SC layer of the skin acts as a barrier, preventing the entry of drugs.[56] Subsequently, FT-IR analysis was conducted to examine changes in the intracellular lipid content within the SC. In general, lipid fluidization and/or lipid extraction from the SC layer are responsible for the enhanced skin permeability of drug molecules.[57] The shift in the CH_2 symmetric and CH_2 asymmetric stretching vibrations at 2858 and 2931 cm^{-1}, respectively, and/or the decrease in the lipid peak area around 2858 cm^{-1} suggest that lipid fluidization and lipid extraction occurred in the SC layer.[58] Additionally, the characteristic keratin peaks for NH–C═O stretching shifted from 1548 cm^{-1} to 1554 cm^{-1} and from 1629 cm^{-1} to 1636 cm^{-1}, indicating that the keratin structure is damaged following patch incubation and providing details about the protein structure in the SC (Fig. 4D and E). These findings allow us to conclude that the drug enters the body by (i) disrupting the lipid bilayers of SC and (ii) altering the structure of the keratin protein. In doing so, it decreases the skin barrier characteristics of the SC, which improves the permeation of the drug into the skin.

3.3. *In vitro* cytotoxicity of hydrogels

The 5-FU-free hydrogels demonstrated outstanding biocompatibility, showing minimal cytotoxicity toward normal cells (data shown above). An *in vitro* cytotoxicity study was conducted to assess the efficacy and dosage needed for 5-FU-loaded hydrogels for tumor cell inhibition.[59] For this purpose, we employed A431 (skin cancer) and MCF-7 (breast cancer) cell lines. The IC_{50} values obtained for the 5-FU@G1 hydrogel after 48 hours were 11.65 μg mL^{-1} for the A431 cell line and 6.44 μg mL^{-1} for the MCF-7 cell line, as illustrated in Fig. 5A and B. Similarly, the IC_{50} values for the 5-FU@G2 hydrogel were 12.23 μg mL^{-1} and 6.51 μg mL^{-1} for the A431 and MCF-7 cell lines, respectively (Fig. 5A and B). These results imply that systems have good cytotoxicity against malignant cell lines at lower dosages (Fig. 5).

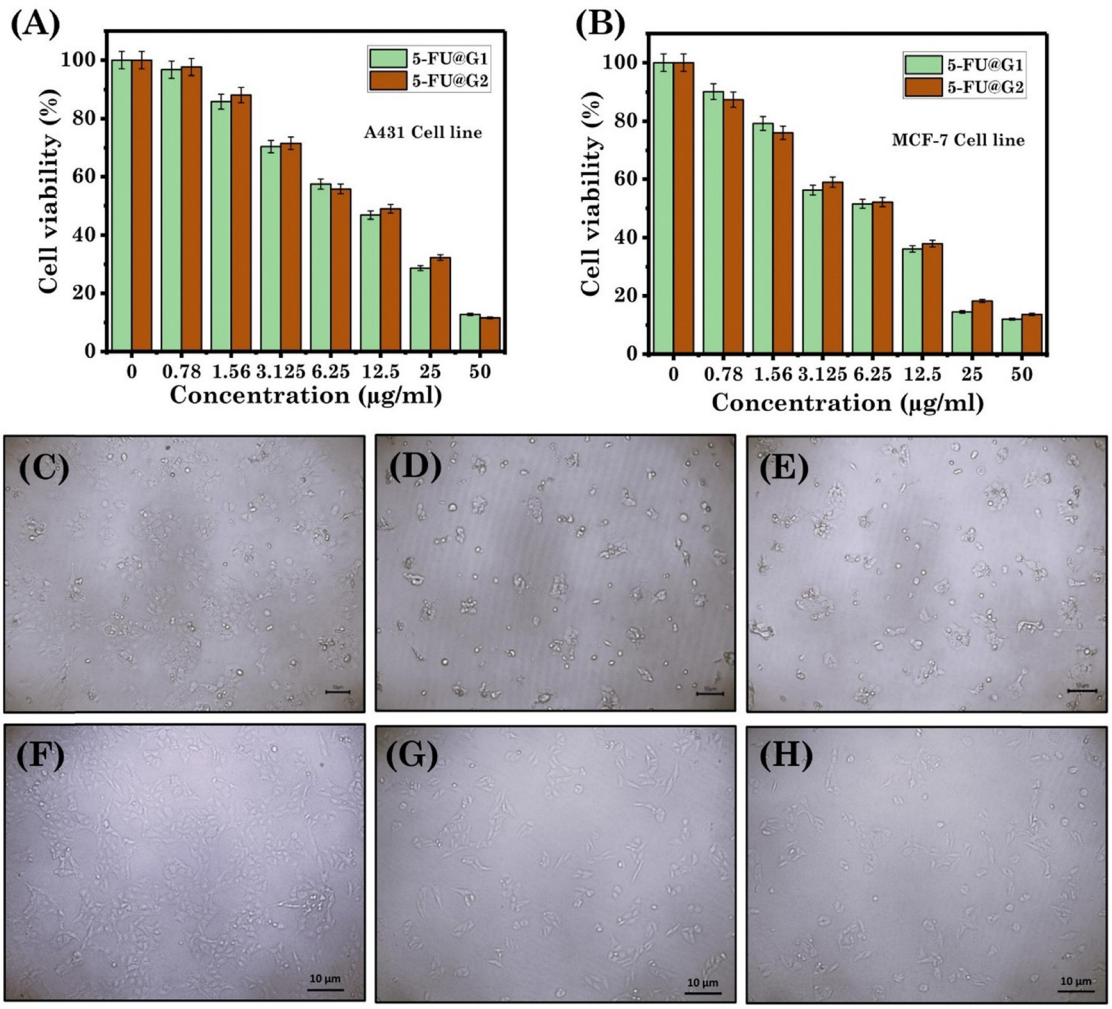

Fig. 5 *In vitro* cytotoxicity of 5-FU-loaded hydrogels on the (A) A431 cell line and (B) MCF-7 cell line; images of the A431 cell line: (C) control and after treatment with (D) 5-FU@G1 and (E) 5-FU@G2; images of the MCF-7 cell line: (F) control and after treatment with (G) 5-FU@G1 and (H) 5-FU@G2.

4. Conclusions

In the present study, we have successfully synthesized [TMG][Ol]@UIO-66-NH_2 composites by incorporating different concentrations of [TMG][Ol]. The IL@MOF composites were then transformed into a hydrogel matrix using CMC-Na as the gelator. The prepared hydrogels can be used as potential multifunctional systems for advanced drug delivery applications, offering a promising combination of structural stability, excellent biocompatibility and enhanced drug-loading and permeation efficacy. We compared the effects of different ratios of [TMG][Ol] in the micropores of UiO-66-NH_2 on their drug delivery performance, thermal stability and drug permeation capability. We successfully prepared two different IL@MOF-based hydrogels by synergistically interacting [TMG][Ol]@UiO-66-NH_2 composites with CMC-Na and analyzed them using BET, XPS, PXRD, FT-IR, SANS, TGA, DSC and FE-SEM techniques. The IL@MOF-based hydrogel demonstrated several advantageous properties, including high mechanical strength, self-healing, self-adhesion and spreadability, making it a promising candidate for TDD applications. The hydrogels demonstrated excellent *in vitro* biocompatibility, with cell viability remaining above 90% for HaCaT cells after 48 hours of treatment with various hydrogel concentrations. Hydrogels improved the permeability of the hydrophilic drug 5-FU through the skin by increasing the fluidity of the intracellular lipid in the SC layer. Among both hydrogels, the hydrogel with higher [TMG][Ol] loading exhibited greater skin permeability. *In vitro* cytotoxicity data showed that 5-FU-loaded hydrogels exerted a potent anticancer effect on A431 and MCF-7 cell lines, even at lower dosages. In conclusion, the IL@MOF-based hydrogels, with their enhanced skin permeability and biocompatibility, present a promising approach for effective TDD, paving the way for future advancements in targeted therapeutic applications.

Author contributions

Ishani Pandya: conceptualization, methodology, writing---original draft and visualization. Vidhi Joshi: methodology and writing—original draft. Raviraj Pansuriya: methodology and writing—original draft. Naina Raje: methodology and writing—original draft. Mohammed A. Assiri: methodology and writing—original draft. Naved Malek: conceptualization, supervision, writing—review and editing, and funding acquisition. All authors have given approval to the final version of the manuscript.

Conflicts of interest

There are no conflicts to declare.

Data availability

Data will be made available upon request.

Supplementary information (SI) is available. See DOI: https://doi.org/10.1039/d5tb00931f.

Acknowledgements

N. M. acknowledges the financial assistance from the Board of Research in Nuclear Sciences (BRNS) with sanction no. 58/14/10/2024-BRNS and UGC-DAE-CSR for the Collaborative Research Scheme (UDCSR/MUM/AO/CRS-M-997/2023). The authors gratefully acknowledge Dr Debes Ray and Dr Vinod K. Aswal for providing access to the SANS instrument facility at the Solid-State Physics Division, Bhabha Atomic Research Centre, Trombay, Mumbai, India.

References

1 W. Y. Jeong, M. Kwon, H. E. Choi and K. S. Kim, *Biomater. Res.*, 2021, **25**, 24.
2 A. Alkilani, M. T. McCrudden and R. Donnelly, *Pharmaceutics*, 2015, **7**, 438–470.
3 M. R. Prausnitz and R. Langer, *Nat. Biotechnol.*, 2008, **26**, 1261–1268.
4 D. Ramadon, M. T. C. McCrudden, A. J. Courtenay and R. F. Donnelly, *Drug Delivery Transl. Res.*, 2022, **12**, 758–791.
5 I. Pathan and C. Setty, *Trop. J. Pharm. Res.*, 2009, **8**, 2.
6 S. A. Ibrahim and S. K. Li, *Pharm. Res.*, 2010, **27**, 115–125.
7 A. Alkilani, M. T. McCrudden and R. Donnelly, *Pharmaceutics*, 2015, **7**, 438–470.
8 R. Pansuriya, T. Patel, K. Singh, A. Al Ghamdi, N. Kasoju, A. Kumar, S. K. Kailasa and N. I. Malek, *Int. J. Biol. Macromol.*, 2024, **277**, 134112.
9 R. Md Moshikur, I. M. Shimul, S. Uddin, R. Wakabayashi, M. Moniruzzaman and M. Goto, *ACS Appl. Mater. Interfaces*, 2022, **14**, 55332–55341.
10 S. N. Pedro, C. S. R. Freire, A. J. D. Silvestre and M. G. Freire, *Int. J. Mol. Sci.*, 2020, **21**, 8298.
11 I. Pandya, S. Mishra, T. Patel, N. Keppeler, S. Kumar, V. K. Aswal, S. Kumar Kailasa, O. El Seoud and N. I. Malek, *J. Mol. Liq.*, 2024, **409**, 125443.
12 M. Jain, H. Ukani, S. Kumar, V. K. Aswal, S. K. Kailasa, O. A. El Seoud and N. I. Malek, *ChemistrySelect*, 2024, **9**, e202303162.
13 R. Pansuriya, J. Doutch, B. Parmar, S. K. Kailasa, N. Mahmoudi, C. Hoskins and N. I. Malek, *J. Mater. Chem. B*, 2024, **12**, 5479–5495.
14 H. Ukani, N. Parsana, S. Mehra, A. Kumar, I. Khan, M. A. Assiri and N. Malek, *ACS Appl. Eng. Mater.*, 2024, **2**, 2583–2596.
15 R. Md Moshikur, Md. R. Chowdhury, H. Fujisawa, R. Wakabayashi, M. Moniruzzaman and M. Goto, *ACS Sustainable Chem. Eng.*, 2020, **8**, 13660–13671.
16 Y. Yao, X. Zhao, G. Chang, X. Yang and B. Chen, *Small Struct.*, 2023, **4**, 2200187.
17 I. Pandya, O. A. El Seoud, M. A. Assiri, S. Kumar Kailasa and N. I. Malek, *J. Mol. Liq.*, 2024, **395**, 123907.

18 L.-Y. Li, Y.-R. Gao, R. Xue, Y. Shu, J.-H. Wang and Z.-J. Wang, *J. Mater. Chem. B*, 2023, **11**, 6491–6515.
19 L. Su, Q. Wu, L. Tan, Z. Huang, C. Fu, X. Ren, N. Xia, Z. Chen, X. Ma, X. Lan, Q. Zhang and X. Meng, *ACS Appl. Mater. Interfaces*, 2019, **11**, 10520–10531.
20 L.-Y. Li, Y.-R. Gao, R. Xue, Y. Shu, J.-H. Wang and Z.-J. Wang, *J. Mater. Chem. B*, 2023, **11**, 6491–6515.
21 J. B. DeCoste, G. W. Peterson, H. Jasuja, T. G. Glover, Y. Huang and K. S. Walton, *J. Mater. Chem. A*, 2013, **1**, 5642.
22 N. Rabiee, M. Bagherzadeh, M. Heidarian Haris, A. M. Ghadiri, F. Matloubi Moghaddam, Y. Fatahi, R. Dinarvand, A. Jarahiyan, S. Ahmadi and M. Shokouhimehr, *ACS Appl. Mater. Interfaces*, 2021, **13**, 10796–10811.
23 Z. Li, S. Zhao, H. Wang, Y. Peng, Z. Tan and B. Tang, *Colloids Surf., B*, 2019, **178**, 1–7.
24 H. Pitakjakpipop, R. Rajan, K. Tantisantisom, P. Opaprakasit, D. D. Nguyen, V. A. Ho, K. Matsumura and P. Khanchaitit, *Biomacromolecules*, 2022, **23**, 365–376.
25 N. Rakhshani, N. Hassanzadeh Nemati, A. R. Saadatabadi and S. K. Sadrnezhaad, *J. Drug Delivery Sci. Technol.*, 2021, **66**, 102881.
26 Ö. Durak, H. Kulak, S. Kavak, H. M. Polat, S. Keskin and A. Uzun, *J. Phys.: Condens. Matter*, 2020, **32**, 484001.
27 I. Pandya, O. A. El Seoud, M. A. Assiri, S. Kumar Kailasa and N. I. Malek, *J. Mol. Liq.*, 2024, **395**, 123907.
28 N. Parsana, O. El Seoud, A. Al-Ghamdi, N. Kasoju and N. Malek, *ChemistrySelect*, 2024, **9**, e202304157.
29 H. F. Xiang, B. Yin, H. Wang, H. W. Lin, X. W. Ge, S. Xie and C. H. Chen, *Electrochim. Acta*, 2010, **55**, 5204–5209.
30 M. Zeeshan, V. Nozari, M. B. Yagci, T. Isık, U. Unal, V. Ortalan, S. Keskin and A. Uzun, *J. Am. Chem. Soc.*, 2018, **140**, 10113–10116.
31 S. Wang, Y. Liu, L. He, Y. Sun, Q. Huang, S. Xu, X. Qiu and T. Wei, *Chin. J. Chem. Eng.*, 2024, **69**, 47–55.
32 X. Chen, X. Wang and D. Fang, *Fullerenes, Nanotubes, Carbon Nanostruct.*, 2020, **28**, 1048–1058.
33 X. Zhao, G. Chang, H. Xu, Y. Yao, D. Dong, S. Yang, G. Tian and X. Yang, *ACS Appl. Mater. Interfaces*, 2024, **16**, 7364–7373.
34 Y. Peng, Z. Chen, R. Zhang, W. Zhou, P. Gao, J. Wu, H. Liu, J. Liu, A. Hu and X. Chen, *Nanomicro. Lett.*, 2021, **13**, 192.
35 N. Rakhshani, N. Hassanzadeh Nemati, A. Ramazani Saadatabadi and S. K. Sadrnezhaad, *Int. J. Eng.*, 2021, **34**, 1874–1881.
36 P. K. Khatri, M. S. Aathira, G. D. Thakre and S. L. Jain, *Mater. Sci. Eng., C*, 2018, **91**, 208–217.
37 H. M. Khalid, A. Mujahid, A. Ali, A. L. Khan, M. Saleem and R. M. Santos, *Int. J. Energy Res.*, 2024, **2024**, 2107340.
38 S. K. Agrawal, N. Sanabria-DeLong, P. R. Jemian, G. N. Tew and S. R. Bhatia, *Langmuir*, 2007, **23**, 5039–5044.
39 B. Hammouda, D. L. Ho and S. Kline, *Macromolecules*, 2004, **37**, 6932–6937.
40 Z. Li, C. Liu, J. J. Frick, A. K. Davey, M. N. Dods, C. Carraro, D. G. Senesky and R. Maboudian, *Carbon*, 2023, **201**, 561–567.
41 J. Shanahan, D. S. Kissel and E. Sullivan, *ACS Omega*, 2020, **5**, 6395–6404.
42 B. Kumar, R. Priyadarshi, Sauraj, F. Deeba, A. Kulshreshtha, K. K. Gaikwad, J. Kim, A. Kumar and Y. S. Negi, *Gels*, 2020, **6**, 49.
43 Y.-Y. Zhang, W. Xu, J.-F. Cao, Y. Shu and J.-H. Wang, *Anal. Chim. Acta*, 2021, **1147**, 144–154.
44 I. Pandya, S. Kumar, V. K. Aswal, O. El Seoud, M. A. Assiri and N. Malek, *Int. J. Pharm.*, 2024, **658**, 124206.
45 H. Jung, M. K. Kim, J. Y. Lee, S. W. Choi and J. Kim, *Adv. Funct. Mater.*, 2020, **30**, 2004407.
46 E. P. Yalcintas, D. S. Ackerman, E. Korkmaz, C. A. Telmer, J. W. Jarvik, P. G. Campbell, M. P. Bruchez and O. B. Ozdoganlar, *Pharm. Res.*, 2020, **37**, 33.
47 W. Pan, W. Wang, P. Wang, D. Chen, S. Liu, L. Zhang, Z. Wang, H. Yang, Y. Xie, F. Huang, G. Zhou and B. Wang, *Mater. Des.*, 2024, **238**, 112688.
48 B. Pardini, R. Kumar, A. Naccarati, J. Novotny, R. B. Prasad, A. Forsti, K. Hemminki, P. Vodicka and J. Lorenzo Bermejo, *Br. J. Clin. Pharmacol.*, 2011, **72**, 162–163.
49 R. Neupane, S. H. S. Boddu, M. S. Abou-Dahech, R. D. Bachu, D. Terrero, R. J. Babu and A. K. Tiwari, *Pharmaceutics*, 2021, **13**, 960.
50 T. Jiang, T. Wang, T. Li, Y. Ma, S. Shen, B. He and R. Mo, *ACS Nano*, 2018, **12**, 9693–9701.
51 M. A. Safwat, G. M. Soliman, D. Sayed and M. A. Attia, *Mol. Pharm.*, 2018, **15**, 2194–2205.
52 R. Neupane, S. H. S. Boddu, J. Renukuntla, R. J. Babu and A. K. Tiwari, *Pharmaceutics*, 2020, **12**, 152.
53 Md. R. Islam, Md. R. Chowdhury, R. Wakabayashi, N. Kamiya, M. Moniruzzaman and M. Goto, *Pharmaceutics*, 2020, **12**, 392.
54 Y. Funakoshi, Y. Iwao, S. Noguchi and S. Itai, *Chem. Pharm. Bull.*, 2015, **63**, 731–736.
55 R. Pansuriya, T. Patel, S. Kumar, V. K. Aswal, N. Raje, C. Hoskins, S. K. Kailasa and N. I. Malek, *ACS Appl. Bio. Mater.*, 2024, **7**, 3110–3123.
56 D. Yang, C. Liu, D. Ding, P. Quan and L. Fang, *Int. J. Pharm.*, 2021, **602**, 120560.
57 A. Banerjee, K. Ibsen, Y. Iwao, M. Zakrewsky and S. Mitragotri, *Adv. Healthcare Mater.*, 2017, **6**, 1601411.
58 R. Md Moshikur, I. M. Shimul, S. Uddin, R. Wakabayashi, M. Moniruzzaman and M. Goto, *ACS Appl. Mater. Interfaces*, 2022, **14**, 55332–55341.
59 M. A. Safwat, G. M. Soliman, D. Sayed and M. A. Attia, *Mol. Pharm.*, 2018, **15**, 2194–2205.